EDGE ARTICLE

Check for updates

All publication charges for this article
have been paid for by the Royal Society
of Chemistry

Synthesis of carbon-supported sub-2 nanometer bimetallic catalysts by strong metal–sulfur interaction†

Shi-Long Xu, [a] Shan-Cheng Shen,[a] Shuai Zhao,[a] Yan-Wei Ding,[a] Sheng-Qi Chu,[b] Ping Chen, [c] Yue Lin [*a] and Hai-Wei Liang [*a]

Small-sized bimetallic nanoparticles that integrate the advantages of efficient exposure of the active metal surface and optimal geometric/electronic effects are of immense interest in the field of catalysis, yet there are few universal strategies for synthesizing such unique structures. Here, we report a novel method to synthesize sub-2 nm bimetallic nanoparticles (Pt–Co, Rh–Co, and Ir–Co) on mesoporous sulfur-doped carbon (S–C) supports. The approach is based on the strong chemical interaction between metals and sulfur atoms that are doped in the carbon matrix, which suppresses the metal aggregation at high temperature and thus ensures the formation of small-sized and well alloyed bimetallic nanoparticles. We also demonstrate the enhanced catalytic performance of the small-sized bimetallic Pt–Co nanoparticle catalysts for the selective hydrogenation of nitroarenes.

1.   Introduction

Bimetallic alloyed nanoparticles (NPs), a solid solution of two metal elements on the nanoscale, have received considerable interest due to their widespread application in electronics, engineering, and particularly catalysis.[1–4] The difference in the catalytic properties of bimetallic NPs compared to their monometallic counterparts derives from the distinct ensemble and electronic structures induced by alloying as well as the synergistic effects between the two metal elements.[5] On the other hand, extremely dispersed metals on porous supports recently emerged as a novel type of high-performance catalyst, containing ultrafine monometallic NPs and even atomically dispersed metals.[6–9] These materials show unprecedented catalytic performance with the decrease of metal particle size, which is associated with their two particular merits: (i) maximizing the metal atom utilization and consequently increasing the activity normalized to mass and/or (ii) regulating the metal electronic properties that are highly dependent on the particle size particularly below 2 nm, due to the quantum size effect and surface effect.[10]

Nevertheless, an inherent problem of small-sized NPs of <2 nm is their well-documented thermodynamic instability,[11–13] as metal species strongly tend to aggregate into larger particles due to the sharply increased surface free energy with the decrease of particle size.[14] This intrinsic drawback makes it extremely challenging to prepare small-sized bimetallic NPs by the conventional impregnation process, in which the elevated reduction temperature that is imperative to guarantee the alloy formation, however, gives rise to severe metal aggregation.[14–16]

To date, several promising approaches have been developed for the synthesis of small-sized bimetallic NPs, typically including colloidal synthesis[17–21] and organometallic precursor methods.[22–24] The organic capping agents used in the colloidal synthesis often block the active metal surface; the complete removal of capping agents normally relies on the thermal treatment above 300 °C. Although direct thermolysis of organometallic cluster complexes provides a strategy for finely controlled synthesis of small-sized alloys at the atomic level, the availability of organometallic precursors is very limited. Very recently, strong electrostatic adsorption[25] and surface inorganometallic chemistry[26] were reported to achieve the general synthesis of small-sized bimetallic NPs. The key to these methods is the use of positively charged metal–amine complexes as metal precursors that electrostatically interact with negatively charged silica supports. The metal loadings in these studies were limited by the adsorption capacity of metal–amine complexes on silica.

Here, we report a novel method to synthesize sub-2 nm bimetallic NPs on mesoporous sulfur-doped carbon (S–C) supports (Fig. 1). Our synthetic strategy is based on the strong chemical interaction between metals and the sulfur atoms that

ᵃHefei National Laboratory for Physical Sciences at the Microscale, Department of Chemistry, University of Science and Technology of China, Hefei, 230026, China. E-mail: hwliang@ustc.edu.cn; linyue@ustc.edu.cn

ᵇInstitute of High Energy Physics, Chinese Academy of Sciences, Beijing, 100049, China

ᶜSchool of Chemistry and Chemical Engineering, Anhui University, Hefei, Anhui 230601, China

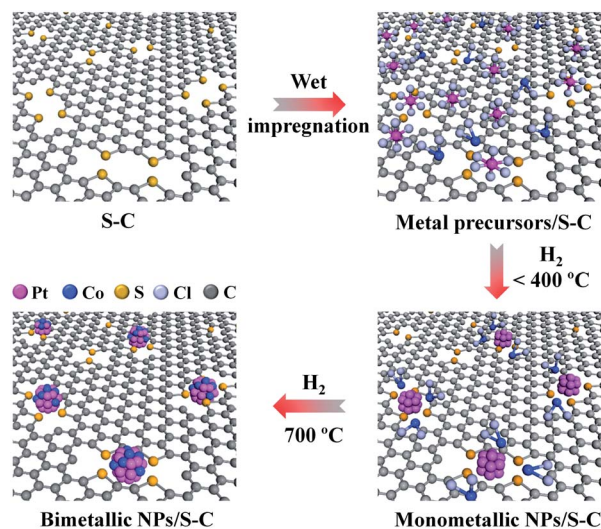† Electronic supplementary information (ESI) available. See DOI: 10.1039/d0sc02620d

Fig. 1 Schematic illustration of the formation process of sub-2 nm bimetallic NPs on the S−C supports.

are doped in the carbon matrix. Such a strong chemical metal–S interaction greatly suppresses the metal aggregation even at an elevated temperature of 700 °C and thus enables us to prepare well alloyed and small-sized bimetallic NPs by the conventional impregnation process with common metal salt precursors. Although some efforts have been made toward the synthesis of atomically dispersed metals or mono/bimetallic NPs on carbon supports, for example, by forming defects *via* ion sputtering,[27–30] modifying with functional groups[31] or doping heteroatoms,[32–37] there are few reports on the general synthesis of small-sized bimetallic NPs of <2 nm on carbon supports.[38]

2. Results and discussion

The S–C supports were first prepared by the cobalt-assisted pyrolysis of a molecular precursor (that is, 2,2′-bithiophene) with silica nanoparticles as templates at 800 °C, after which the silica template and cobalt species were removed by NaOH and H_2SO_4 etching, respectively.[39] Transmission electron microscopy (TEM) and N_2 sorption tests indicated the mesoporous nature of S–C with a high specific surface area of 1324 m^2 g^{-1} (Fig. S1a and b†). Importantly, the S–C supports possessed a high content of sulfur atoms (S/C ratio of 0.08) doped in the carbon matrix (Table S1†), mainly in the form of a C–S–C structure (Fig. S1c†). These structural features enable the S–C supports to afford a large number of easily accessible sulfur sites for fixing metal species.

We then demonstrated the synthesis, characterization, and formation mechanism of the sub-2 nm bimetallic NPs on the S–C supports by taking Pt–Co as a typical example. Bimetallic Pt–Co NPs were prepared by a conventional impregnation method that involved the wet-impregnation of common metal salt precursors (that is, H_2PtCl_6 and $CoCl_2$) on the S–C supports and a subsequent H_2 (5 vol% H_2/Ar) reduction process (Fig. 1). To guarantee a high alloying degree in the bimetallic NPs, we carried out the H_2-reduction at a relatively high temperature of

700 °C. The total metal (Pt + Co) loading for the bimetallic catalysts was controlled to be 5 wt% with certain metal mole ratios.

Powder X-ray diffraction (PXRD) patterns show a small drum pack around 40.3° (Fig. S1d†). The peak shifts to higher angles, relative to the (111) planes of pure Pt metal (39.7°), indicating that Co atoms are incorporated into the fcc Pt lattice to form an alloy phase with a concomitant lattice contraction.[40] The broad peak at around 23° 2θ is assigned to the S–C supports with a low graphitization degree. Consistent with the PXRD results, high-angle annular dark-field scanning transmission electron microscopy (HAADF-STEM) observations in a large field of view showed no metal NPs (Fig. 2a). In the high-magnification HAADF-STEM images, we observed numerous small-sized metal clusters with an average size of 1.4 nm (Fig. 2b and c), which were homogeneously dispersed over the whole carbon matrix.

For comparison, we carried out control syntheses by using two commercial high-surface-area carbon black samples (Vulcan XC72R and Ketjen Black EC-300J, abbreviated as V-72R and K-300J, respectively) as supports by the same process. HAADF-STEM observations showed a number of large particles of >20 nm dispersed over the carbon black supports, suggesting that the mixed metal pair underwent serious sintering during the high-temperature H_2-reduction. To further confirm the crucial role of the doped sulfur atoms in the synthesis, we removed the sulfur atoms efficiently from the pristine S–C support by annealing it in 5 vol% H_2/Ar at 1000 °C for 2 h and then prepared Pt–Co bimetallic NPs with the desulfurated S–C by the same process. With the significant decrease of the S/C ratio from 0.08 to 0.01 for the S–C supports (Table S1†) after the high-temperature desulfurization treatment, a broader particle size distribution of Pt–Co NPs was found on the desulfurated S–C support (Fig. 2f). These control syntheses definitely certified the pivotal role of the doped sulfur atoms in suppressing metal aggregation.

The energy-dispersive X-ray spectroscopy (EDS) element-mapping technique can directly image the distribution of metal species in NPs, but the imaging of small-sized particles of <2 nm
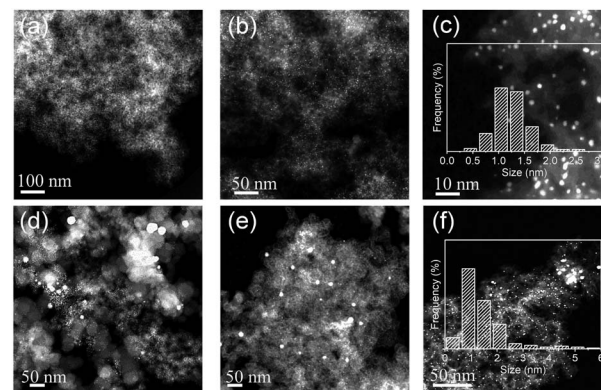

Fig. 2 HAADF-STEM images of Pt−Co bimetallic NPs supported on S−C (a−c), V-72R (d), K-300J (e), and the desulfurated S−C support (f). The insets in (c) and (f) are the size distributions of the corresponding samples.

is highly challenging.[25,41] Here we fortunately got the distinct EDS mapping images of Pt–Co bimetallic NPs (Fig. 3a). Within each individual nanoparticle, Pt and Co elements were homogeneously distributed, which indicated that the sub-2 nm clusters were well alloyed. EDS line scan analyses supplied additional evidence for the co-existence of two metal elements in individual NPs for the Pt–Co sample (Fig. 3b). The difference of particle size between the EDS line-scan and HAADF-STEM could be ascribed to the instrument sensitivity and sample vibration under the electron beam.[26,42] Further, the atomic structures of the Pt–Co NPs were further revealed by aberration-corrected HAADF-STEM imaging. In line with the literature,[25] the Z-contrast difference of Pt and Co atoms could be observed clearly (Fig. 3c). Obviously, we observed amorphous or poorly crystalline clusters consisting of loosely assembled metal atoms for the Pt–Co catalyst. The lattice spacing of 2.20 Å can be indexed to the (111) planes of the Pt–Co alloyed NPs.

The above PXRD and HAADF-STEM results definitely verify that the prepared Pt–Co nanoparticles exist as a disordered bimetallic alloy rather than an ordered intermetallic alloy, although ordered Pt_3Co nanoparticles could be prepared at a similar temperature with commercial carbon black supports.[40] We suppose that the strong metal–S interaction would suppress not only the inter-particle sintering but also the intra-particle atom ordering, thus restraining the formation of ordered structures. Further, according to the Pt–Co binary phase diagram (as shown in Fig. S2†), in our case the Co/Pt ratio of 2 is far away from the ideal stoichiometric ratio of intermetallic $L1_0$-type PtCo or $L1_2$-type Pt_3Co, which will greatly reduce the thermodynamic driving force toward the ordered phase. In addition, the high surface energy of the small sized Pt–Co nanoparticles of less than 2 nm will also lower the driving force for disordered–ordered conversion.[3]

Further, we performed the temperature-programmed reduction (TPR) to verify the close proximity of Pt and Co for the

Pt–Co bimetallic sample (Fig. 3d). TPR profiles show that monometallic Pt and Co can be reduced at around 178 and 394 °C, respectively. In the case of bimetallic Pt–Co, the first peak at around 191 °C is assigned to the reduction of Pt or the formation of the Pt–Co alloy, while the second peak at around 309 °C is from the reduction of monometallic Co. The significant shift of the TPR peak of Co reduction to low temperature in the bimetallic Pt–Co sample can be attributed to the hydrogen spillover from Pt to unreduced Co salts, which is indicative of the close proximity of Pt–Co atoms.[25,43,44]

To verify the strong metal–sulfur interaction and understand the formation process of small-sized bimetallic NPs on S–C, we performed X-ray photoelectron spectroscopy (XPS), X-ray absorption near edge structure (XANES) and extended X-ray fine structure (EXAFS) analyses of the Pt–Co catalysts obtained at 200, 400, and 700 °C, respectively. We observed a strong Cl 2p signal in the XPS survey (Fig. 4a) for the H_2PtCl_6–$CoCl_2$/S–C composite precursor, which receded significantly after H_2-reduction at 200 °C. Raising the H_2-reduction temperature to above 400 °C could remove all Cl ligands from the metal precursor. These results are in line with the TPR analyses that both Pt and Co species could be efficiently reduced by H_2 at 400

Fig. 4 Formation process of small-sized bimetallic NPs on S–C. (a) XPS survey spectra of the bimetallic Pt–Co system before and after H_2-reduction at different temperatures. (b) XANES spectra of bimetallic Pt–Co and reference samples at the Pt L_3 edge. (c) XPS spectra of the Pt 4f region of the bimetallic Pt–Co system before and after H_2-reduction at different temperatures. (d) Fourier transforms of EXAFS spectra of bimetallic Pt–Co and reference samples at the Pt L_3 edge. (e) EDS elemental mapping of Pt–Co/S–C prepared at different temperatures, illustrating the evolution process of Pt–Co NPs.
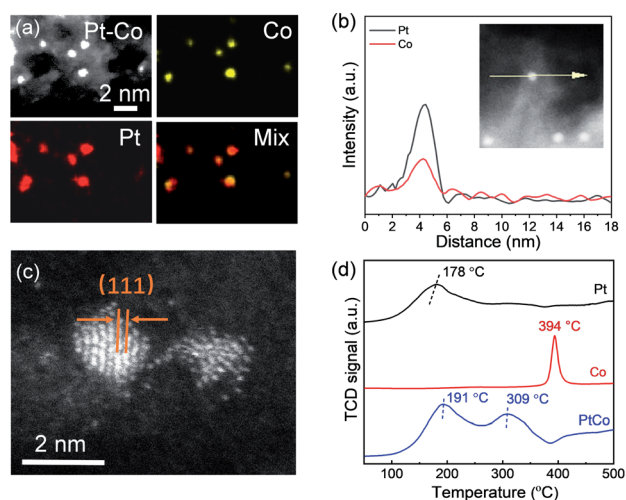

Fig. 3 Characterization of Pt–Co bimetallic NPs on S–C. (a) EDS elemental mapping. (b) EDS line scan. (c) Atomic resolution HAADF-STEM image. (d) TPR of monometallic Pt and Co and bimetallic Pt–Co on the S–C supports.
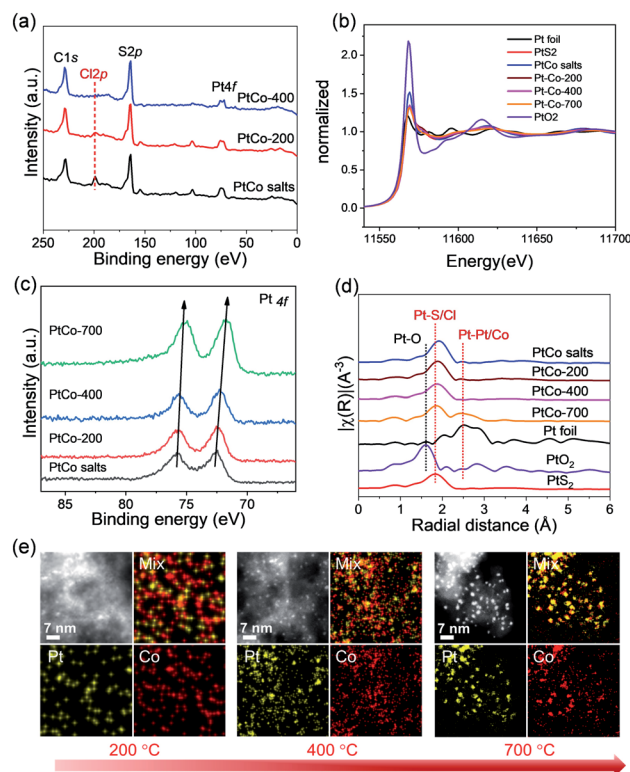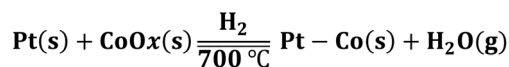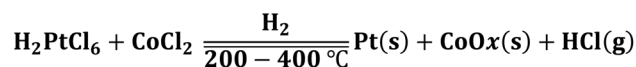
°C. It is worth noting that there were still considerable sulfur atoms left in the carbon support (S/C ratio of 0.03) even after the H_2-reduction at 700 °C (Table S1†). We surmise that these surviving sulfur atoms play a pivotal role in tethering the metal species and preventing them from severe sintering at high temperature.

In the normalized XANES spectra recorded at the Pt L_3-edge, the shape and intensity of Pt–Co/S–C (200–700 °C) are close to those of PtS_2 (Fig. 4b), indicating that the coordination environment of Pt atoms is similar to that of PtS_2. The white-line intensity of Pt–Co decreased steadily with the increase of the H_2-reduction temperature (Fig. 4b). The changing pattern of the white-line intensity is well consistent with that of the Pt 4f peak position in XPS spectra, which shifts from 72.45 eV for the H_2PtCl_6–$CoCl_2$/S–C precursor to 71.70 eV for the Pt–Co/S–C catalysts formed at 700 °C (Fig. 4c). These results reflect the gradually decreased oxidation state of Pt with the increase of the reduction temperature. The Fourier-transformed (FT) k_3-weighted EXAFS spectra of Pt for the Pt–Co catalysts prepared at different temperatures are presented in Fig. 4d. The spectra of Pt foil, PtO_2, and PtS_2 are also shown for comparison. All Pt–Co samples exhibit a prominent peak at *ca.* 1.8 Å, which is associated with the first shell of Pt–S or Pt–Cl scattering. EXAFS cannot distinguish the coordinated S and Cl atoms, because they give similar scattering parameters due to their nearest atomic number.[45] The above XPS analyses indicate that all Cl ligands have left the S–C support when the H_2-reduction temperature reached 400 °C, while the doped sulfur atoms in the carbon matrix can be stable even at 700 °C. We therefore assign the 1.8 Å peak exclusively to Pt–S bonds for PtCo-400 and PtCo-700. Moreover, a new peak at *ca.* 2.5 Å appears for the PtCo-700 catalyst, corresponding to Pt–Pt or Pt–Co scattering. The Co K-edge EXAFS spectra suggest that Co predominantly coordinates with oxygen instead of sulfur for all Pt–Co samples, and that the metallic coordination corresponding to Co–Co or Co–Pt starts to form at 400 °C (Fig. S3a†). We note that the presence of Co–O and Pt–S bonds as revealed by the above XANES/EXAFS analyses is reasonable considering that Pt has a strong tendency to bond with S at the nanoparticles/S–C interface and that the Co atoms in the particles will be oxidized quickly when exposed to air. Further, the fraction of atoms located at the particle surface and at the particle/support interface will be dominant for the small-sized particles. For example, for a 1.1 nm Pt nanoparticle, the fraction of surface Pt atoms could be as high as 60%.[46] In such a case, it is challenging to differentiate the metallic bonds in the XANES/EXAFS analyses.

The EDS mapping technique was then used to study the evolution of Pt and Co element distribution on the S–C support with the increase of H_2-reduction temperature (Fig. 4e). At a low temperature of 200 °C, both Pt and Co elements are highly dispersed on the whole carbon matrix, without Pt or Co element concentration on the nanoscale. When the temperature was increased to 400 °C, Pt and Co elements are partially overlapped, revealing the tendency of bimetallic NPs. At a high temperature of 700 °C, Pt and Co elements are almost completely overlapped and concentrated in the particle region, indicating the formation of highly alloyed NPs.

On the basis of the above analyses, we figure out that the strong metal–sulfur interaction plays a pivotal role in the synthesis of small-sized alloyed NPs on the S–C supports. As schematically illustrated in Fig. 1, at a low temperature (*e.g.* 200 °C), the sulfur-containing sites on S–C serve as nucleation centers for Pt reduction *via* the Pt–S bonds. At an elevated temperature (*e.g.* 400 °C), the Co species have the propensity to nucleate on the reduced Pt surfaces driven by the hydrogen spillover effect,[25] forming the bimetallic assembled structures with proximal Pt and Co atoms. A further increase of the temperature to 700 °C results in the reorganization of the Pt/Co assemblies into well alloyed nanoparticles.[16,40] Benefiting from the high thermal stability of the doped sulfur atoms in S–C and the strong Pt–S interaction, the aggregation and ripening of bimetallic Pt–Co NPs are greatly suppressed even at 700 °C, eventually leading to the formation of alloyed nanoclusters. In brief, the possible chemical equations have been speculated to express the whole reaction process as shown below:

$$H_2PtCl_6 + CoCl_2 \xrightarrow[200-400\,°C]{H_2} Pt(s) + CoOx(s) + HCl(g)$$

$$Pt(s) + CoOx(s) \xrightarrow[700\,°C]{H_2} Pt-Co(s) + H_2O(g)$$

To validate the generality of this approach, we extended this strong metal–S interaction strategy to other metal pairs, such as $IrCl_3$–$CoCl_2$ and $RhCl_3$–$CoCl_2$. The bonding of metal with sulfur was also confirmed in the Rh–Co and Ir–Co bimetallic systems by EXAFS (Fig. S3b and c†). HAADF-STEM images reveal the presence of finely size-controlled metal nanoclusters with sizes of 1.4 ± 0.3 and 0.9 ± 0.3 nm, respectively (Fig. 5a, S4 and S5†). EDS mapping images indicate that noble metals (Rh and Ir) and Co elements are co-located in every particle, which is direct visual evidence of good alloying (Fig. 5b).

Note that the recently reported strong electrostatic adsorption[25] and surface inorganometallic chemistry methods[26] are limited by the availability of suitably charged metal complex precursors (for example, cationic ammonia complexes). Differently, the versatility of the sulfur-confined strategy enabled us to use common metal precursors for the synthesis of bimetallic nanoclusters, including organometallic platinum complexes ($Pt(acac)_2$), Pt-containing cations ($Pt(NH_3)_4(OH)_2$) or anions (H_2PtCl_6), and various Co salts, such as $CoCl_2$, $Co(NO_3)_2$, CoC_2O_4, and $CoSO_4$, as confirmed by the EDS line scan and PXRD measurements (Fig. S6 and S7†). In addition, the structural features of the S–C supports, that is, high surface area and abundant sulfur anchoring sites, allow for a high-metal-loading synthesis (Table S3†). We did not observe any aggregation or overgrowth of Pt–Co nanoclusters even when the total metal loading was increased to 10 and 20 wt% (Fig. S8†). EDS line scan analyses confirmed the alloyed structure for these high-loading samples (Fig. S9†).
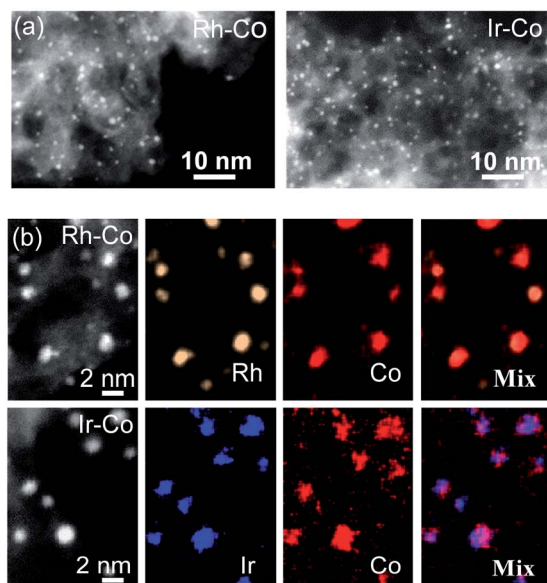
Fig. 5 (a) HAADF-STEM images of Rh–Co and Ir–Co bimetallic NPs. (b) EDS elemental mapping of Rh–Co and Ir–Co bimetallic NPs.

Next, we studied the selective hydrogenation of nitroarenes on the prepared small-sized Pt–Co NP catalysts to demonstrate their utility. Selective conversion of nitroarenes to anilines by catalytic hydrogenation is industrially important, as aniline and its derivatives are key feedstocks in fine chemical, agrochemical, and pharmaceutical industries.[47] We chose the selective hydrogenation of *p*-chloronitrobenzene to *p*-chloroaniline as the model reaction to evaluate the catalytic performance of bimetallic Pt–Co catalysts (Fig. S10†). Pd, Pt, and Ir are well known to be very active for the hydrogenation process, but the undesired C–Cl bond breaking is difficult to circumvent on monometallic catalysts particularly at high conversion rates.[48,49] As expected, our kinetics studies showed that the commercial Pt/C catalysts tend to produce the by-product aniline through the undesirable over-hydrogenation even before the complete conversion (Fig. S11a†). Although S–C supported monometallic Pt showed better tolerance to over-hydrogenation, we still detected the formation of aniline when the conversion was close to 100% (Fig. S11b†). Remarkably, the introduction of various amounts of Co to form a Pt–Co alloy on the S–C supports could completely 'switch-off' the dechlorination reaction even for a prolonged reaction time (Fig. S11c–e†). The monometallic Co did not show any activity, indicating that Pt is the active site for this reaction.

We then compared the catalyst activity by calculating the turnover frequency (TOF). The *p*-chloronitrobenzene conversion was maintained below 30% in all cases to ensure that the reaction remained under kinetic control. Interestingly, the TOF of the bimetallic Pt–Co catalysts gradually increased from 478 h^{-1} to 1589 h^{-1} with the increase of the Pt/Co atomic ratio from 1 to 5 (Fig. 6a), approaching that of monometallic Pt/C (1814 h^{-1}) and Pt/S–C catalysts (1789 h^{-1}). These results demonstrate that alloying of Pt with only a small amount of Co leads to a remarkably improved selectivity, meanwhile almost retaining

the high activity of monometallic Pt. The Pt–Co/K-300J (Pt/Co = 5) bimetallic catalyst displayed a substantially lower TOF of 943 h^{-1}, probably due to the inhomogeneous particle size distribution of Pt–Co on the carbon black support (Fig. S11d and S12†). We ascribe the high catalytic performance of Pt–Co/S–C to the small size and electronic effects induced by alloying, which change the adsorption behavior of *p*-chloronitrobenzene primed for preferential reduction of the nitro group[50,51] and suppression of C–Cl dissociation.[49]

The durability of the bimetallic Pt–Co catalysts was then established by intermittent cycling tests. After five cycles, the catalyst exhibited undiminished activity and selectivity (Fig. 6b). Both PXRD analysis and HAADF-STEM observation revealed no morphology change of the catalysts (Fig. S13–S15†), illustrating the high stability of the small-sized alloyed NPs on the S–C supports. Other nitroarene compounds containing –C=C, –C=O, –C≡N, and halogen functional groups were also amenable to selective hydrogenation with the bimetallic Pt–Co/S–C catalysts (Table S6†).

We note that a metal–organic framework-derived N-doped carbon with a similar high specific surface area (1230 m^2 g^{-1}) to our S–C support (1324 m^2 g^{-1}) was reported recently to act as a support to prepare a bimetallic Pt–Co nanoparticle catalyst.[51] The parallel comparison of this reported work with ours as listed in Table S7† clearly demonstrates the superiority of the S–C support over the N-doped carbon for fixing small-sized bimetallic nanoparticles. A higher catalytic activity of Pt–Co/S–C than Pt–Co/N–C was also found for the hydrogenation of 1-chloro-2-nitrobenzene, probably due to the exposure of more active surface metal atoms for the small sized Pt–Co nanoparticles on the S–C supports.

Generally, sulfur is normally recognized as a poison reagent for metal catalysts, as the active metal surface can be blocked by the adsorption of sulfur-containing species.[52,53] Differently, in our case, the S elements are doped in the carbon matrix mainly in the form of C–S–C bonds (Fig. S1c†). After the deposition of metal nanoparticles on the S–C supports, the metal nanoparticle surface should be S-free and accessible for catalysis, even though at the metal/S–C interface a few metal atoms bond
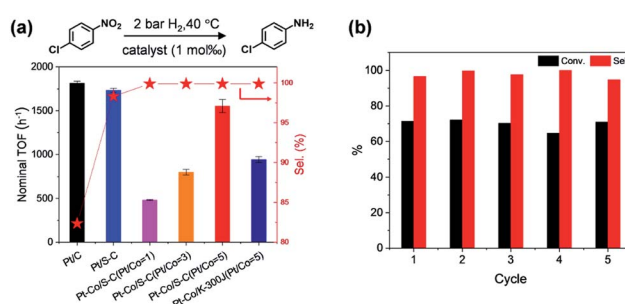

Fig. 6 Catalytic performance of Pt–Co bimetallic NPs for nitroarene hydrogenation. (a) TOF and selectivity for *p*-chloroaniline of Pt–Co/S–C and reference catalysts. (b) Recycling experiments over five runs for Pt–Co/S–C (Pt/Co = 5). Note that the selectivity (a) and recycling experiments (b) were chosen at 2.0 h and 30 min, respectively. Reaction conditions: 3 mmol substrate, 1 mol‰ Pt catalyst, methyl alcohol, 2 bar H$_2$, 40 °C.

with S to form the metal–S–C configuration. Besides, the previous studies reported by us[36,37] and another group[32] have demonstrated that the doped sulfur in carbon supports did not poison the supported monometallic Pt and Ir nanoparticle catalysts for catalytic hydrogenation and electrocatalysis.

3. Conclusion

In summary, we have demonstrated a simple and general method to synthesize M–Co (M = Pt, Rh, Ir) sub-2 nm bimetallic NPs with a size of less than 2 nm. Our methodology is based on the strong metal–sulfur interaction that suppresses metal sintering at high temperature and ensures the formation of small-sized and well alloyed bimetallic NPs on the S–C supports. The enhanced catalytic performance of the small-sized bimetallic nanoparticle catalysts was evidenced in the selective hydrogenation of nitroarenes. Our results serve as impetus to the catalysis field in terms of the design and synthesis of advanced bimetallic or multimetallic catalysts. Further, we suppose that the sulfur-fixing synthesis strategy could be extended to the synthesis of small-sized intermetallic ordered nanoparticle catalysts at evaluated temperatures.

Conflicts of interest

There are no conflicts to declare.

Acknowledgements

Notes and references

1 O. S. Alexeev and B. C. Gates, *Ind. Eng. Chem. Res.*, 2003, **42**, 1571–1587.

2 P. Buchwalter, J. Rosé and P. Braunstein, *Chem. Rev.*, 2014, **115**, 28–126.

3 Y. Yan, J. S. Du, K. D. Gilroy, D. Yang, Y. Xia and H. Zhang, *Adv. Mater.*, 2017, **29**, 1605997.

4 T. Ghosh, B. M. Leonard, Q. Zhou and F. J. DiSalvo, *Chem. Mater.*, 2010, **22**, 2190–2202.

5 A. K. Singh and Q. Xu, *ChemCatChem*, 2013, **5**, 652–676.

6 X.-F. Yang, A. Wang, B. Qiao, J. Li, J. Liu and T. Zhang, *Acc. Chem. Res.*, 2013, **46**, 1740–1748.

7 L. Liu and A. Corma, *Chem. Rev.*, 2018, **118**, 4981–5079.

8 S. Mitchell, E. Vorobyeva and J. Pérez-Ramírez, *Angew. Chem., Int. Ed.*, 2018, **130**, 15538–15552.

9 P. Liu, Y. Zhao, R. Qin, S. Mo, G. Chen, L. Gu, D. M. Chevrier, P. Zhang, Q. Guo, D. Zang, B. Wu, G. Fu and N. Zheng, *Science*, 2016, **352**, 797–800.

10 M. A. El-Sayed, *Acc. Chem. Res.*, 2004, **37**, 326–333.

11 J. Chai, X. Liao, L. R. Giam and C. A. Mirkin, *J. Am. Chem. Soc.*, 2012, **134**, 158–161.

12 S. H. P. Joo, J. Young, C.-K. Tsung, Y. Yamada, P. Yang and G. A. Somorjai, *Nat. Mater.*, 2009, **8**, 126–131.

13 H. Chen, Y. Yu, H. L. Xin, K. A. Newton, M. E. Holtz, D. Wang, D. A. Muller, H. D. Abruña and F. J. DiSalvo, *Chem. Mater.*, 2013, **25**, 1436–1442.

14 C. T. Campbell, S. C. Parker and D. Starr, *Science*, 2002, **298**, 811–814.

15 A. Cao and G. Veser, *Nat. Mater.*, 2010, **9**, 75–81.

16 N. J. LiBretto, C. Yang, Y. Ren, G. Zhang and J. T. Miller, *Chem. Mater.*, 2019, **31**, 1597–1609.

17 R. W. Scott, A. K. Datye and R. M. Crooks, *J. Am. Chem. Soc.*, 2003, **125**, 3708–3709.

18 R. W. Scott, O. M. Wilson, S.-K. Oh, E. A. Kenik and R. M. Crooks, *J. Am. Chem. Soc.*, 2004, **126**, 15583–15591.

19 N. Toshima, *J. Macromol. Sci., Chem.*, 1990, **27**, 1225–1238.

20 H. Zhang, T. Watanabe, M. Okumura, M. Haruta and N. Toshima, *Nat. Mater.*, 2012, **11**, 49–52.

21 M. Takahashi, H. Koizumi, W.-J. Chun, M. Kori, T. Imaoka and K. Yamamoto, *Sci. Adv.*, 2017, **3**, e1700101.

22 A. Kulkarni and B. C. Gates, *Angew. Chem., Int. Ed.*, 2009, **48**, 9697–9700.

23 S. Chotisuwan, J. Wittayakun, R. J. Lobo-Lapidus and B. C. Gates, *Catal. Lett.*, 2007, **115**, 99–107.

24 A. S. Fung, M. J. Kelley, D. C. Koningsberger and B. C. Gates, *J. Am. Chem. Soc.*, 1997, **119**, 5877–5887.

25 A. Wong, Q. Liu, S. Griffin, A. Nicholls and J. R. Regalbuto, *Science*, 2017, **358**, 1427–1430.

26 K. Ding, D. A. Cullen, L. Zhang, Z. Cao, A. D. Roy, I. N. Ivanov and D. Cao, *Science*, 2018, **362**, 560–564.

27 A. V. Nartova, A. V. Bukhtiyarov, R. I. Kvon, E. M. Makarov, I. P. Prosvirin and V. I. Bukhtiyarov, *Surf. Sci.*, 2018, **677**, 90–92.

28 D. V. Demidov, I. P. Prosvirin, A. M. Sorokin and V. I. Bukhtiyarov, *Catal. Sci. Technol.*, 2011, **1**, 1432–1439.

29 M. Favaro, L. Perini, S. Agnoli, C. Durante, G. Granozzi and A. Gennaro, *Electrochim. Acta*, 2013, **88**, 477–487.

30 A. V. Bukhtiyarov, I. P. Prosvirin and V. I. Bukhtiyarov, *Appl. Surf. Sci.*, 2016, **367**, 214–221.

31 Y.-T. Kim and T. Mitani, *J. Catal.*, 2006, **238**, 394–401.

32 C. H. Choi, M. Kim, H. C. Kwon, S. J. Cho, S. Yun, H. T. Kim, K. J. J. Mayrhofer, H. Kim and M. Choi, *Nat. Commun.*, 2016, **7**, 10922.

33 N. Cheng, S. Stambula, D. Wang, M. N. Banis, J. Liu, A. Riese, B. Xiao, R. Li, T.-K. Sham, L.-M. Liu, G. A. Botton and X. Sun, *Nat. Commun.*, 2016, **7**, 13638.

34 L. Perini, C. Durante, M. Favaro, V. Perazzolo, S. Agnoli, O. Schneider, G. Granozzi and A. Gennaro, *ACS Appl. Mater. Interfaces*, 2015, **7**, 1170–1179.

35 H. I. Lee, S. H. Joo, J. H. Kim, D. J. You, J. M. Kim, J.-N. Park, H. Chang and C. Pak, *J. Mater. Chem.*, 2009, **19**, 5934–5939.

36 L. Wang, M.-X. Chen, Q.-Q. Yan, S.-L. Xu, S.-Q. Chu, P. Chen, Y. Lin and H.-W. Liang, *Sci. Adv.*, 2019, **5**, eaax6322.

37 Q.-Q. Yan, D.-X. Wu, S.-Q. Chu, Z.-Q. Chen, Y. Lin, M.-X. Chen, J. Zhang, X.-J. Wu and H.-W. Liang, *Nat. Commun.*, 2019, **10**, 4977.

38 Y.-T. Kim, H. Lee, H.-J. Kim and T.-H. Lim, *Chem. Commun.*, 2010, **46**, 2085–2087.

39 Z.-Y. Wu, S.-L. Xu, Q.-Q. Yan, Z.-Q. Chen, Y.-W. Ding, C. Li, H.-W. Liang and S.-H. Yu, *Sci. Adv.*, 2018, **4**, eaat0788.

40 D. Wang, H. L. Xin, R. Hovden, H. Wang, Y. Yu, D. A. Muller, F. J. DiSalvo and H. D. Abruña, *Nat. Mater.*, 2013, **12**, 81–87.

41 T. Iida, D. Zanchet, K. Ohara, T. Wakihara and Y. Román-Leshkov, *Angew. Chem., Int. Ed.*, 2018, **57**, 6454–6458.

42 M. W. Small, S. I. Sanchez, L. D. Menard, J. H. Kang, A. I. Frenkel and R. G. Nuzzo, *J. Am. Chem. Soc.*, 2011, **133**, 3582–3591.

43 L. Chen, A. C. Cooper, G. P. Pez and H. Cheng, *J. Phys. Chem. C*, 2007, **111**, 18995–19000.

44 W. Karim, C. Spreafico, A. Kleibert, J. Gobrecht, J. VandeVondele, Y. Ekinci and J. A. van Bokhoven, *Nature*, 2017, **541**, 68–71.

45 X. Li, W. Bi, L. Zhang, S. Tao, W. Chu, Q. Zhang, Y. Luo, C. Wu and Y. Xie, *Adv. Mater.*, 2016, **28**, 2427–2431.

46 B. Zhang, H. Asakura, J. Zhang, J. Zhang, S. De and N. Yan, *Angew. Chem., Int. Ed.*, 2016, **55**, 8319–8323.

47 N. Ono and H. Feuer, *The Nitro Group in Organic Synthesis*, Wiley-VCH, New York, 2001.

48 H. Wei, X. Liu, A. Wang, L. Zhang, B. Qiao, X. Yang, Y. Huang, S. Miao, J. Liu and T. Zhang, *Nat. Commun.*, 2014, **5**, 5634.

49 S. Iihama, S. Furukawa and T. Komatsu, *ACS Catal.*, 2015, **6**, 742–746.

50 Y. Peng, Z. Geng, S. Zhao, L. Wang, H. Li, X. Wang, X. Zheng, J. Zhu, Z. Li, R. Si and J. Zeng, *Nano Lett.*, 2018, **18**, 3785–3791.

51 H. Yang, S. J. Bradley, A. Chan, G. I. N. Waterhouse, T. Nann, P. E. Kruger and S. G. Telfer, *J. Am. Chem. Soc.*, 2016, **138**, 11872–11881.

52 J.-R. Chang, S.-L. Chang and T.-B. Lin, *J. Catal.*, 1997, **169**, 338–346.

53 J.-R. Chang and S.-L. Chang, *J. Catal.*, 1998, **176**, 42–51.